An Improved Method for Localization of Wireless Capsule Endoscope Using Direct Position Determination

ALI ESHKEVARI[ID] **AND SEYED MOHAMMAD SAJAD SADOUGH**[ID]
Faculty of Electrical Engineering, Shahid Beheshti University, Tehran 1983969411, Iran

Corresponding author: Seyed Mohammad Sajad Sadough (s_sadough@sbu.ac.ir)

ABSTRACT A novel methodology for localization of wireless-capsule-endoscope (WCE) by using the direct-position-determination (DPD) method is proposed. A WCE enables the diagnose of gastrointestinal tract disorders in a non-invasive visual manner. Conventional methods proposed for WCE localization are not optimal in terms of positioning accuracy since they include two *disjoint* stages: **i)** estimation of initial parameters such as direction, time, or time-difference of arrival (DOA, TOA, TDOA), and **ii)** localization performed by intersecting the loci provided by initial parameters. Moreover, most of these methods can localize only one signal transmitter. In contrast, the considered DPD is a single-step method which processes data from all sensor elements simultaneously and can resolve several (theoretically one less than sensors number) co-channel signal sources in a medical ward. More precisely, the proposed method can concurrently localize a WCE and some beacons attached to the patient's body, which can supersede the use of micro-electromechanical-systems (MEMS). In addition, the considered DPD can locate some WCEs for multiple patients at the same time. To do this, DPD seeks for the peaks of a spatial profit function (SPF) which is based on the statistical cumulants of the signals observed at the array sensors placed around the medical ward. Here, we propose the classical DPD (CDPD) as a coarse but fast, and the generalized DPD (GDPD) as a fine and high resolution method for an improved localization of WCE. Also, the proposed technique can be easily extended to any other indoor applications, where the dimensions of the whole monitoring area and receiving array are about some carrier wavelengths. The superiority of CDPD over DOA-based WCE localization technique, and GDPD over CDPD is verified through comprehensive numerical analysis. We have also drawn the Cramer-Rao lower bound (CRLB) as a benchmark for performance analysis of GDPD. Moreover, we introduced a tighter lower bound on the localization mean square error (MSE) achieved with multiple group arrays (MGLB), corresponding to CDPD and DOA-based methods, to show the superiority of GDPD over these techniques.

INDEX TERMS Direct position determination, direction of arrival, sensor array, wireless capsule endoscope, beacon.

I. INTRODUCTION

A. BACKGROUND AND MOTIVATIONS

During the recent decades, there has been a growing interest on the localization of wireless-capsule-endoscope (WCE) by using radio-location techniques in the general context of wireless-medical-telemetry-services (WMTS) [1]–[6]. From the estimation theory point of view, the conventional WCE

localization techniques are sub-optimum since they have two separate and disjoint stages: first, the estimation of some initial parameters such as direction, time, time-difference of arrival (DOA, TOA, TDOA), or the received signal strength (RSS), and second, the intersection of outcome loci from those parameters to localize the target. The direct position determination (DPD) is proposed more recently as a *single-step* optimal technique for multiple co-channel signal localization by jointly using all captured data from sensor elements [7]–[11]. DPD is a statistical approach which uses

---

The associate editor coordinating the review of this manuscript and approving it for publication was Mohammad Zia Ur Rahman[ID].

a *spatial* profit function (SPF) whose peaks indicate the location of the signal transmitters. More precisely, the SPF is the result of a mathematical solution to the localization problem, which is based on the statistical properties of signals sensed at the sensor array, usually their covariance or higher order cumulant matrices [12]. These solutions are commonly referred to as *beamformers* [13]. Nevertheless, the high accuracy of DPD method is achieved at the expense of some extra hardware requirements such as synchronous sampling of signals observed at all sensor elements [7]–[10].

B. LITERATURE SURVEY

The positioning accuracy of WCE using received-signal-strength (RSS) technique is investigated in [1], [4]. A DOA-based WCE localization technique by using an unscented Kalman filter is studied in [2], [14] in a scenario where the patient can move freely in the medical ward while a micro-electromechanical-system (MEMS) is used to recognize the body location and orientation. A performance and complexity analysis for a DOA/TOA/TDOA based WCE radio-location system with circular arrays is presented in [3]. More recently, a WCE localization based on the measurement of the magnetic field [5], and a two-way TOA oriented WCE radio-location technique utilizing finite-element-method simulations [6] are proposed, where both techniques use a free shaped array on the patient's belly. However, the aforementioned bi-step radio-location methods are neither theoretically optimum nor can resolve co-channel signals. To the best of our knowledge, no DPD-based WCE or other biomedical sensor-based radio localization is proposed so far [15]–[18].

On the other hand, there are few works in classical DPD (CDPD) literature regarding indoor applications including WMTS or more specifically WCE localization. In their pioneering work [7], Weiss *et al.* considered a tactical field application, and showed that DPD coincides exactly with the maximum-likelihood (ML) estimation. In [8], [10], DPD is employed using different beamformers such as minimum-variance-distortionless-response (MVDR) and multiple-signal-classification (MUSIC), respectively. A performance analysis of DPD with both MVDR and MUSIC beamformers is addressed in [9], [11]. Some DPD applications for wideband systems like radar and orthogonal frequency-division multiplexing (OFDM) is provided in [19], [20]. More specifically, a performance analysis of DPD using MUSIC algorithm is presented in [21].

C. CONTRIBUTIONS

As shown in FIGURE 1, we define two types of array structures which will be used throughout this paper. More precisely, FIGURE 1-(a) shows the multiple-group-array (MGA) and FIGURE 1-(b) depicts the single-group-array (SGA), where the former is commonly-used in DOA-based radio location techniques. The main contributions of this paper for localization of a WCE and/or some beacons attached to the patient as an instance of WMTS, are summarized as follows.
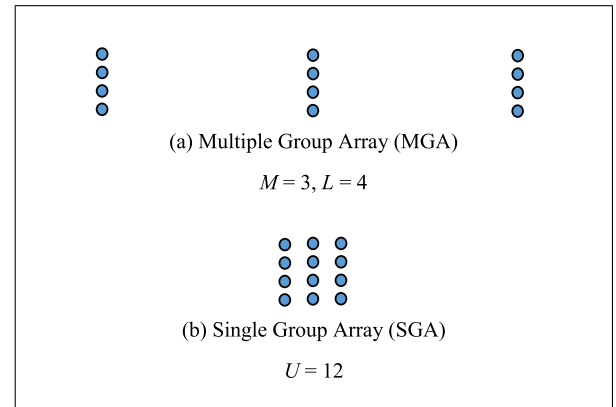

FIGURE 1. (a) MGA and (b) SGA array structures.

- We propose the CDPD, which is an optimum localization technique as an alternative to the commonly-used DOA-based techniques, both using the same MGA structure. CDPD is a medium resolution technique since it ignores statistical relations between received signals from any two different sensor groups.
- We propose the generalized DPD (GDPD) as a high resolution localization technique compared to CDPD, using an SGA antenna structure with the capability of simultaneous sampling on all sensor elements. Although GDPD provides us with a very higher accuracy than CDPD, it may suffer from some spurious peaks in SPF while locating emitters with co-channel signals.
- We show that our previously introduced technique called dynamic-sensor-array-response (DSAR) [22] can be used to effectively reduce the mentioned spurious peaks of SPF in GDPD.
- We introduce a lower bound on localization mean square error (MSE) achieved by MGA antenna structures (MGLB), which is tighter than the Cramer-Rao lower bound (CRLB) that is essentially defined for SGA structures (Appendix A).
- We introduce two visual analysis tools based on CRLB (*CRgram*) and its statistical gradient (*CRgrad*) at each location of the monitoring area, which can be used for visual performance evaluation.
- We propose different solutions to combat and decrease the fading effect due to multi-path propagation.
- We investigate the wave refraction phenomenon inside the human body and proposed two refraction canceling method based on DPD. First, a pre-cancellation technique that considers the refraction effect throughout the DPD algorithm, and second, a post-cancellation method that removes the estimation bias caused by the refraction (Appendix B) after running the DPD algorithm.

D. PAPER STRUCTURE

The rest of this paper is organized as follows. In Section II, we present the problem formulation for the proposed GDPD

and CDPD methods by considering the commonly-adopted SGA and MGA structures. In Section III, we express the beamformers (SPF makers) that are then used in DPD formalism. In Section V, we compare the localization techniques based on the MGA (for DOA-based and/or CDPD) and SGA (for GDPD) array structures, where we also introduce some visual tools for better arrangement of array elements. In Section VII, we investigate the effect of the human body and the refraction phenomenon due to wave traveling through two different environments. Then, we address the necessary modifications in the system model parameters to limit the refraction problem. In Section VI, we use the proposed localization methods to reduce the fading effect on the DPD algorithm. Subsequently, in Section VIII, we present our simulations and numerical results to validate the superiority of our proposed methods in terms of positioning accuracy and resolution. Finally, we conclude the paper in Section IX.

E. NOMENCLATURE
The following conventions are used throughout this paper.

$\{.\}^*$	Conjugate
$\{.\}^T$	Transpose
$\{.\}^H$	Hermitian (conjugate transpose)
$\{.\}^\dagger$	Pseudo inverse
$*$	Convolution
$\circ$	Hadamard product of matrices
$\otimes$	Kronecker product of matrices
$\times$	Cross product of vectors
$tr(.)$	Trace of a matrix
$diag(.)$	Diagonal matrix
$blkdiag(..)$	Block diagonal matrix
$\|.\|$	Frobenius norm of a matrix
$\mathbb{E}\{.\}$	Statistical expectation
$\boldsymbol{I}_N$	Identity matrix of size $N \times N$
$\boldsymbol{1}_N$	All-one matrix of size $N \times N$
λ	Carrier wavelength
$\boldsymbol{F}$	Fisher Information Matrix (FIM)
$\boldsymbol{J}$	Inverse of the FIM
$\delta(.)$	Dirac delta function

Throughout this paper, the DOA or azimuth angles are considered in navigation, (i.e., clock oriented and not trigonometric) mode.

II. PROBLEM FORMULATION
We consider an MGA with M separated L-element arrays/groups with element spacing about λ. For an indoor application such as a medical ward, the aforementioned MGA can also be considered as an SGA with $U = LM$ sensor elements as depicted in FIGURE 1. We also consider K emitters transmitting uncorrelated co-channel signals. All receiver sensors are assumed to be stationary during the observation time interval, which is much larger than the maximum possible propagation delay over receiver sensors array. Meanwhile, the emitted signals are also assumed stationary

during observation time since this condition can be met by human walking speed through a medical ward. The three dimensional (3D) coordinate vector of k-th transmitter is denoted by $\boldsymbol{p}_k = [x_k, y_k, z_k]^T$ where $k = 1, \ldots, K$. We aim at estimating the unknown positions of K transmitters, based on the observations received by the sensors array. Notice that for a linear time-invariant (LTI) channel with impulse response $h(t)$, the received $x(t)$ corresponding to a narrow-band (NB) source $s(t) = a e^{j2\pi f_c t}$ with a being the amplitude and f_c the center frequency, writes

$$x(t) = h(t) * s(t) = H(f_c)\,s(t),$$

which means that for a NB signal, the convolution reduces to a simple multiplication with channel response at signal's center frequency, which is a complex scalar.

Considering a U-element SGA, we model the channel response between the u-th receiver sensor and the k-th signal emitter as

$$\tilde{a}_{uk}(f_c, \boldsymbol{p}_k) = \alpha_{uk} \cdot a_{uk}(f_c, \boldsymbol{p}_k), \quad u = 1, \ldots, U, \tag{1}$$

where f_c is the carrier frequency and

$$\alpha_{uk} = 1 + \beta_{uk}, \tag{2}$$

indicates the *stochastic* part of the channel response where 1 represents the line-of-site (LOS) received signal component, and β_{uk} is a zero-mean circularly-symmetric complex Gaussian random variable characterizing the fading effect due to multi-path propagation for instance, and finally

$$a_{uk} = g_{uk} e^{-j\delta_{uk}} = g_0 \frac{d_0}{d_{uk}} e^{-j\frac{2\pi}{\lambda}d_{uk}}, \tag{3}$$

denotes the *deterministic* part of channel response, with g_{uk} and δ_{uk} as amplitude and phase responses of the channel respectively, which can be expressed in terms of the channel path-length d_{uk}, and the normalization factors g_0 and d_0. Therefore, the statistical NB signal model can be expressed as

$$x = \widetilde{\boldsymbol{A}}(\boldsymbol{P})s + b, \tag{4}$$

where x and b are vectors of random variables (RV) characterizing the received signal and the generated noise at U sensor elements, respectively, $\boldsymbol{P} = [\boldsymbol{p}_1, \ldots, \boldsymbol{p}_K]^T$ is the coordinates matrix of K transmitters, and s is a vector of RVs denoting the transmitted signals from K emitters. We have

$$\widetilde{\boldsymbol{A}}(\boldsymbol{P}) = \boldsymbol{\alpha} \circ \boldsymbol{A}(\boldsymbol{P}), \tag{5}$$

with $\widetilde{\boldsymbol{A}}$, $\boldsymbol{\alpha}$, and $\boldsymbol{A}$ being the channel response, the fading factors, and the *sensor-array-response* or *pointing* matrices, respectively. The k-th column of array response matrix $\boldsymbol{A}$ that corresponds to the k-th emitter's location, is hereafter referred to as the *pointing vector* a_k. Considering a *slow fading* or a quasi-static channel for this NB model, we can assume $\boldsymbol{\alpha}$ to be constant during the signal observation time interval for each location estimation.

A. CDPD FORMULATION

Considering an MGA structure that is mainly used in DOA-based localization techniques, we propose the CDPD as an improved alternative method that exploits MGA structure, where any statistical relations between observed data in different arrays are ignored. Consequently, the matrix form of (4) for the m-th array will be

$$X_m = \widetilde{A}_m S + B_m, \tag{6}$$

where all scalar RVs in (4) are replaced by their N-sample row vectors and so, RV column vectors x, s, and b in (4) are respectively replaced by matrices X_m, S_m, and B_m. This leads to a least squares estimation (LSE) problem for M distinct arrays as

$$\widehat{P} = \underset{P}{argmin} \sum_{m=1}^{M} \left\| X_m - \widetilde{A}_m(P)S \right\|^2, \tag{7}$$

where $\widehat{P}$ is the estimated locations of K emitters and P is the vector of K *scanning* points through the monitoring area.

B. GDPD FORMULATION

To achieve a method with more resolution than CDPD in an indoor localization application, we propose the GDPD technique that jointly takes into account the statistical dependency of all observations on receiver elements. This means that GDPD considers the SGA structure for all sensors that is based on the generalized form of the (6) as

$$X = \widetilde{A} S + B, \tag{8}$$

where

$$\begin{aligned} X &= [X_1^T, \ldots, X_M^T]^T, \\ \widetilde{A} &= [\widetilde{A}_1^T, \ldots, \widetilde{A}_M^T]^T, \\ B &= [B_1^T, \ldots, B_M^T]^T. \end{aligned} \tag{9}$$

Regarding the statistical dependcy of observations of whole sensor elements in an SGA, the LSE problem will be

$$\widehat{P} = \underset{P}{argmin} \left\| X - \widetilde{A}(P)S \right\|^2, \tag{10}$$

which is a generalized form of (7).

III. LOCALIZATION ALGORITHMS

Obviously, in the estimation problems such as (7) or (10) the $\widetilde{A}$ and S are unknown because we know nothing about the location and number of signal sources. We only can analytically explain the pointing matrix A as a function of K transmitters' locations. This means that at least a $3K$-dimensional search is necessary to find the proper $\widehat{P}$, providing that K is known. To solve such a problem, we first consider (10) for a single transmitter ($K = 1$) and by ignoring the fading effect, we have

$$\hat{p} = \underset{p}{argmin} \left\| X - as \right\|^2, \tag{11}$$

where a is the pointing vector of p, and s is the sample vector of emitted signal. We are looking for an SPF which depends only on the available data X and the scanning point p. To solve such a problem, we can estimate s as a minimizer to the Frobenius norm term in problem (11) which is given by

$$\hat{s} = a^\dagger X = (a^H a)^{-1} a^H X = a^H X, \tag{12}$$

where $a^H a$ is the norm of pointing vector of p that should be normalized during the search of monitoring area ($\|a\| = 1$). From (11) and (12), we have

$$\hat{p} = \underset{p}{argmin} \ tr\left([X - aa^H X]^H [X - aa^H X]\right), \tag{13}$$

and after some manipulations we get

$$\hat{p} = \underset{p}{argmax}(a^H X X^H a). \tag{14}$$

By defining the sample covariance matrix of observations as

$$R \triangleq \frac{1}{N} X X^H, \tag{15}$$

we have

$$\hat{p} = \underset{p}{argmax}(a^H R a), \tag{16}$$

which is the well-known conventional or *Bartlett* beamformer whose output value indicates the received signal power by the array. This was first introduced as a proper solution for DOA estimation of a single transmitter [13], which we use in DPD.

To localize multiple signal emitters, we can exploit many improved beamformers that are originally introduced for DOA estimation of multiple sources. Some of these beamformers are mentioned in next Section. It is worth mentioning that these beamformers usually need the covariance matrix of observations, i.e., R. Thus, we consider this matrix for both CDPD and GDPD cases.

Regarding (15), the general form of observations covariance matrix for the GDPD will be

$$R = \frac{1}{N} X X^H = \widetilde{A} R_S \widetilde{A}^H + R_B, \tag{17}$$

where $R_S \triangleq \frac{1}{N} S S^H$ and $R_B \triangleq \frac{1}{N} B B^H$ denote the covariance matrices of source signals and whole elements noise, respectively.

Using analogy, the covariance matrix of observations for m-th array in CDPD will be

$$R_m = \frac{1}{N} X_m X_m{}^H = \widetilde{A}_m R_S \widetilde{A}_m^H + R_{Bm}, \tag{18}$$

with R_S, and $R_{Bm} = \frac{1}{N} B_m B_m{}^H$ denoting the covariance matrices of source signals and m-th array's noise, respectively. The general form of observations covariance matrix R for CDPD problem is defined as

$$R \triangleq \begin{bmatrix} R_1 & \ldots & 0 \\ \vdots & \ddots & \vdots \\ 0 & \ldots & R_M \end{bmatrix} = blkdiag(R_1, \ldots, R_M), \tag{19}$$

which ignores the statistical dependency of M separated arrays.

A. BEAMFORMERS

All beamformers (SPF-oriented algorithms) proposed the in context of co-channel DOA estimation problems can be exploited in DPD due to the similarity of their problem formulations, for instance, Bartlett [13], Capon or MVDR [23], [24], adaptive angular response (AAR) [25], thermal noise algorithm (TNA) [26], and MUSIC beamformer [27]. In contrast, non-SPF-oriented algorithms such as ROOT-MUSIC and ESPRIT which provide the estimated DOA in a direct mathematical form, cannot be used in DPD. Here we present the formulations of some commonly-used beamformers as

$$SPF_{Bartlett} = a^H \boldsymbol{R} a, \tag{20}$$

$$SPF_{MVDR} = (a^H \boldsymbol{R}^{-1} a)^{-1}, \tag{21}$$

$$SPF_{MUSIC} = (a^H \boldsymbol{Q}\boldsymbol{Q}^H a)^{-1}, \tag{22}$$

where $a = a(\boldsymbol{p})$ is the *pointing vector* of point $\boldsymbol{p}$ that scans throughout the monitoring area to find the peaks of the SPF, one-by-one. Considering the uniform definitions of $\boldsymbol{R}$ for CDPD and GDPD, the solutions are uniquely formulated as

$$\hat{\boldsymbol{p}}_k = \underset{\boldsymbol{p}}{\operatorname{argmax}} \; SPF\,(a(\boldsymbol{p}), \boldsymbol{R}) \,, \tag{23}$$

where $k = 1, \ldots, K$, and $\hat{\boldsymbol{p}}_k$ is the estimated position of k-th signal emitter.

IV. CONSIDERATIONS ABOUT CONVENTIONAL WCE LOCALIZATION SCENARIOS

In a WCE lab such as that depicted in FIGURE 2, the first step of conventional localization technique is determining the DOA of the WCE signal by using each column (group) of sensors array around the WMTS ward, independently [2]. The second step is the estimation of intersection points of loci presented by each column array to estimate the WCE position. This is aided by using MEMS beacons positions to find the WCE location in the patient's body frame. An unscented Kalman filter is then used to improve target tracking while the patient walks through the medical ward.

In contrast, our proposed CDPD and GDPD techniques, whose flowchart is depicted in FIGURE 3, localize the WCE in a single-step search. It can also obviate the need of using MEMS components, which yields a unified localization hardware.

Regardless of the localization technique, there are some considerations about this WCE lab specifications [2], that should be taken into account.

1) The distance between patient and each column arrays is not so long compared to the length of that array (2.5 m) to let us consider the array response as a function of DOA only. Therefore, the DOA-based localization contains an inevitable error in this scenario.
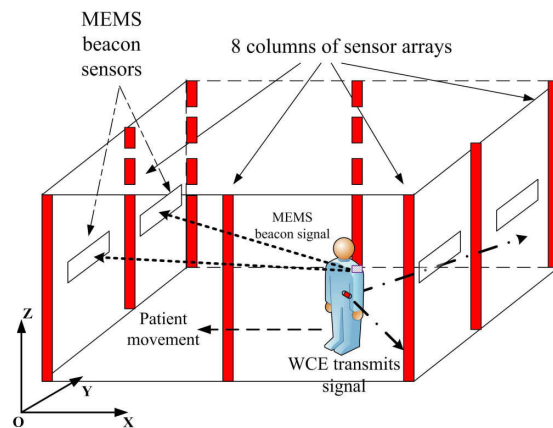2) The sensor elements spacing b, is a more important parameter than the length of array. The optimum value

FIGURE 2. The WCE localization scenario in [2] using a DOA-based method aided by a MEMS system, in a WMTS ward with dimensions 10 m × 5 m × 2.5 m.
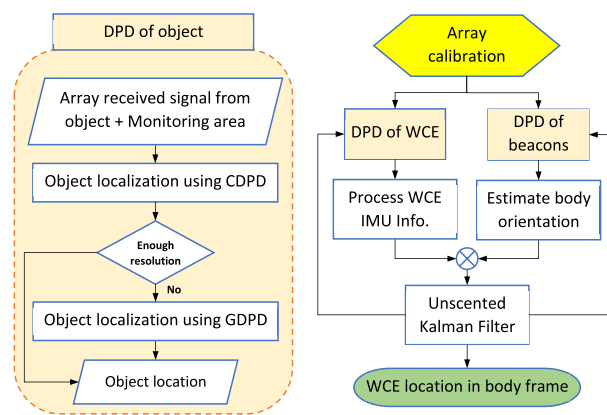

FIGURE 3. Flowchart of our proposed WCE localization algorithm in a WMTS ward.

depends on λ and on the array geometry [13], which means that the array length may not be constant in contrast to the scenario in [2] which uses 3, 5, 7, or 10 sensors per column array with a length of 2.5m.

3) The far-field condition is violated through the WCE localization scenario mentioned in [2] since $\lambda \simeq 21$ cm for the standard 1430 MHz carrier frequency, while the distance from the walking patient can be less than $10\lambda = 2.1$m.

V. COMPARING LOCALIZATION METHODS BASED ON MGA AND SGA STRUCTURES

It is obvious that in a localization problem, we expect a higher resolution and accuracy while using an SGA structure (for GDPD) compared to using an MGA (for CDPD), since the mutual information between different groups (arrays) is ignored in the latter. On the other hand, although both DOA-based localization techniques and CDPD exploit MGA structures, the CDPD performs very closer to MGLB since it jointly uses the information from all groups together in a single stage [7]. Therefore, we do not deal with the details
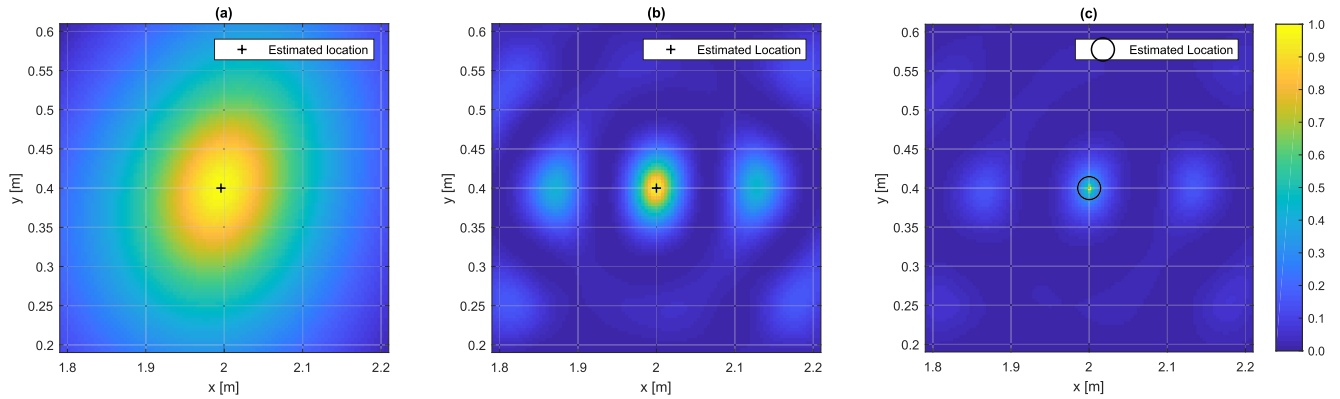
FIGURE 4. Qualitative comparison of normalized SPFs of CDPD, GDPD (high-resolution, with spurs), and GDPD+DSAR (ultra-resolution, dimmed spurs); the emitter is located at (2, 0.4, 0) m inside the monitoring area with dimensions 2λ × 2λ.
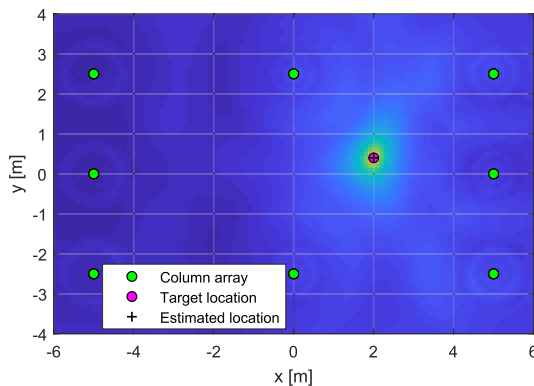

FIGURE 5. The smooth heat map of SPF for CDPD as a medium resolution (coarse) localization method, for plane z = 0; the emitter is located at (2, 0.4, 0) m.

of DOA-based localization methods here, and only compare CDPD as the best MGA-oriented technique to GDPD.

We also consider that the GDPD may suffer from unwanted spurious peaks on its SPF, and show that our previously proposed DSAR technique can efficiently reduce these spurs from the SPF of GDPD.

A. A QUALITATIVE COMPARISON
FIGURE 4 shows the details of a transmitter localization, through which we can qualitatively compare the normalized SPFs of (a) CDPD that is smooth and low-resolution, (b) GDPD presenting higher resolution but with possible spurious peaks around the target, and (c) GDPD+DSAR showing an ultra-high-resolution surface and also a high-contrast between the true peak and spurs. The DSAR method considers the free-space-loss (FSL) through the elements of pointing matrix A to provide a more realistic channel model. Also, FIGURE 5 depicts the general 2D heat map of CDPD SPF whose peak determines the location of signal emitter.

B. AN ANALYTIC COMPARISON: THEORETICAL LOWER BOUNDS
To compare the proposed methods in terms of positioning accuracy, we derived the CRLB and MGLB for GDPD and

CDPD problems respectively in Appendix A, and showed that MGLB is a tighter lower bound (LB) than CRLB. We know that the inverse of the Fisher Information Matrix ($J = F^{-1}$) contains the lower limits for covariance between each pair of parameters $\psi = [x, y, z]^T$ as

$$\sigma_{\psi_i \psi_j} \triangleq [J]_{ij} \leq \text{cov}(\hat{\psi}_i, \hat{\psi}_j). \tag{24}$$

To compare the performance of CDPD and GDPD, we consider the MGLB and CRLB respectively, for up to three transmitters in some arbitrary points on a horizontal plane in WTMS ward, namely (0,0,0)m, (2,0.4,0)m, and (2,-0.4,0)m. FIGURE 6 depicts the RMSE LBs normalized to wavelength λ at point (0,0,0)m for a signal source there, while one or two other sources are emitting at other points. FIGURE 7 shows the RMSE LBs at point (2,0.4,0)m with the same scenario. Comparing these two plots, it can be easily figured out that:

- The theoretical resolution of GDPD is about 15 dB better than that of CDPD, which is due to the fact that GDPD exploits the whole covariance matrix R elements, while CDPD ignores the mutual information between different groups.
- GDPD is robust to the presence of multiple signal transmitters and also to the location of evaluation point through the monitoring area, while CDPD does not show such a robustness. Notice that the theoretical limit for number of signal sources is one less than the number of sensor elements in a group [13], which is L for CDPD and $U = LM$ for GDPD.

The aforementioned characteristics encourage us to propose the combination of CDPD and GDPD for localization of multiple biomedical sensors in a WMTS environment. It is worth mentioning that although GDPD has a very higher resolution than CDPD, it requires a huge computational burden without prior usage of CDPD as a coarse position estimator.

C. VISUAL TOOLS FOR ARRAY ARRANGEMENT ANALYSIS: CRgram AND CRgrad
Here, we introduce some visual analysis tools for finding the proper array geometry, using the elements of matrix J. For
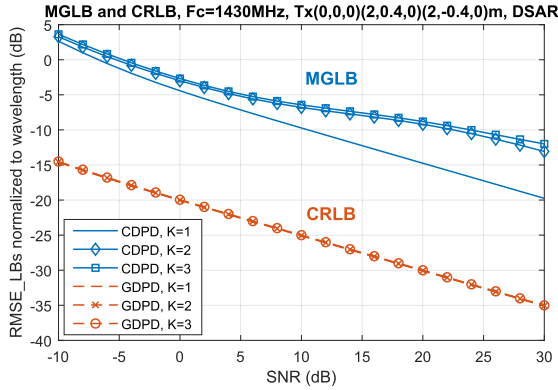
FIGURE 6. The normalized LBs of RMSE at point (0, 0, 0) m for K transmitters in 1–3 mentioned points, regarding CDPD and GDPD.
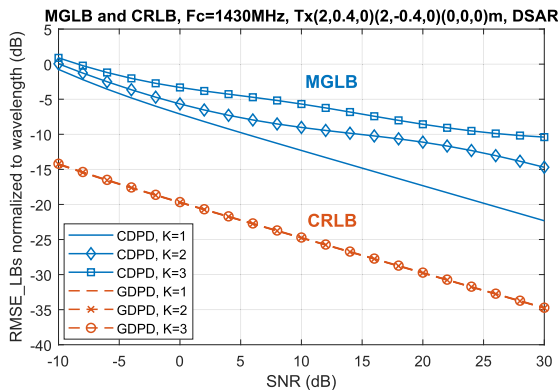

FIGURE 7. The normalized LBs of RMSE at point (2, 0.4, 0) m for K transmitters in 1–3 mentioned points, regarding CDPD and GDPD.
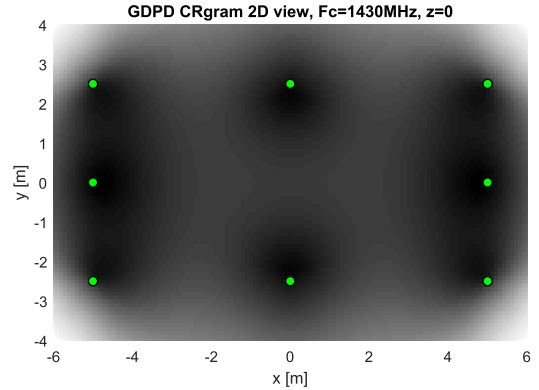

FIGURE 8. The 2D view of *CRgram* in the WMTS ward array for plane $z = 0$; the green circles show the column array locations. Darker points indicate lower localization errors.
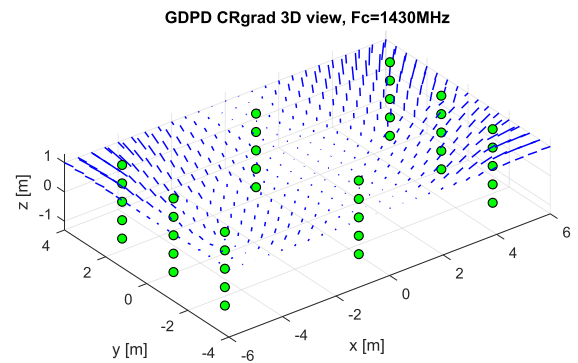

FIGURE 9. The 3D view of *CRgrad* in the WMTS ward array for plane $z = 1$; the green circles show the elements of array, and lines show the gradient of localization error at each point.

any arbitrary location in the monitoring area, the CRLB is determined by computing $tr(\boldsymbol{J})$ which involves only main diagonal elements $[\boldsymbol{J}]_{ii} = \sigma_{\psi_i}^2$. In fact, the set of CRLB values for all grid points in a 2D monitoring area can make a surface or an image to show the quality of estimation at that location. We refer to the heat-map of this surface as the array Cramer-Rao-gram (*CRgram*) (see FIGURE 8). According to the gray color-map, the darker color indicates a lower error. Although the CRLB can be calculated for a 3D area, such an image can only be achieved for a 2D cut of the monitoring area usually perpendicular to one of the Cartesian axes $\{x, y, z\}$.

To provide a 3D analysis tool, we propose a line-based plot whose lines show the magnitude and direction of gradient of localization error. This plot uses the non-diagonal elements of $\boldsymbol{J}$ in addition to the diagonal ones. We define $\boldsymbol{u}$ as the CRLB gradient unit vector as

$$\boldsymbol{u} \triangleq \frac{[\sigma_x, \sigma_y, \sigma_z]^T}{\left\| [\sigma_x, \sigma_y, \sigma_z] \right\|}, \tag{25}$$

and $\boldsymbol{g}$ as the CRLB gradient vector as

$$\boldsymbol{g} \triangleq \frac{\left\| [\rho_{xy}, \rho_{xz}] \right\|}{\sqrt{2}} \text{ sign} \left([1, \rho_{xy}, \rho_{xz}]^T \right) \circ \boldsymbol{u}, \tag{26}$$

whose magnitude shows the *mutual dependency* of error distribution on the Cartesian axes, where ρ is the Pearson correlation coefficient, defined as

$$\rho_{\psi_i \psi_j} \triangleq \frac{\sigma_{\psi_i \psi_j}}{\sigma_{\psi_i} \sigma_{\psi_j}}. \tag{27}$$

We denote the resulted view or picture as *array CRgrad* (see FIGURE 9). Moreover, the combination of *CRgram* and *CRgrad* can be exploited as a visual tool to assess the error associated to an array, such as that depicted in FIGURE 10.

VI. REDUCING THE EFFECT OF CHANNEL FADING

To reduce deterioration due to the multipath fading channel, the first step consists in performing some physical regularities in the medical ward e.g., by covering the medical equipment with radiation absorbing materials [2]. In this way, the LOS signal becomes stronger than the reflections leading to less localization errors. The second step can be accomplished using mathematical techniques to compensate the fading impact. In Section II, we modeled the fading effect as a random factor in the channel response matrix, inspired by the model proposed by Weiss *et al.* in their pioneering
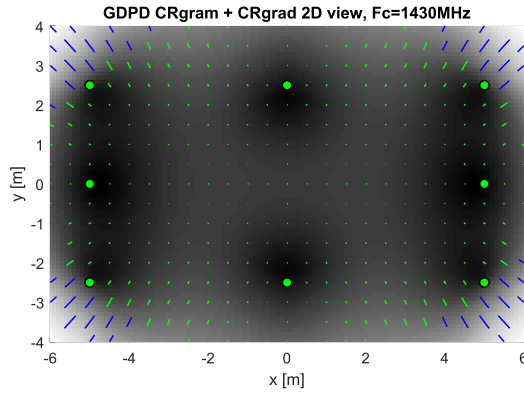
FIGURE 10. The 2D combination of CRgram and CRgrad of WMTS ward array for plane $z = 0$; the green circles show the column array locations. The CRgrad lines colors are adapted to the background for a better look.

works [7]–[9]. We have

$$\alpha_{uk} = CN(1, \sigma_f^2), \qquad (28)$$

where $u = 1, \ldots, U$ and $k = 1, \ldots, K$, and α_{uk} is a circular complex Gaussian random variable with mean one and standard deviation σ_f (*fading depth*), drawn independently per u-th sensor and k-th emitter (i.e., per each channel path). considering a *Rician fading channel* for each path we have

$$\mathbb{E}\{\alpha_{uk}\} = 1. \qquad (29)$$

It is worth mentioning that we assume slow fading or quasi-static channels in such a way that each α_{uk} can be treated as a constant during each observation time interval for one DPD procedure. We modeled the fading effect in our system model in Section II, by Hadamard multiplying the fading factor matrix $\boldsymbol{\alpha} = [\alpha_{uk}]$ to array response (pointing matrix) $\boldsymbol{A}$. According to (29), it is clear that averaging can asymptotically neutralize the fading coefficients to a constant value. Assuming that DPD is an unbiased estimator, we propose three possible averaging-oriented schemes to overcome the fading effect: first, the averaging over coordinates (Avg_*p*), second, the averaging over pointing vector (Avg_*a*) of each estimated location (both with heavy computational loads), and third and most important one, the averaging over covariance matrix $\boldsymbol{R}$ (Avg_*R*) which we discuss as follows.

A. AVERAGING OVER COVARIANCE MATRIX R

Considering (5) and (17), and assuming uncorrelated noise at receivers the sample covariance matrix of observations is

$$\boldsymbol{R} = (\boldsymbol{\alpha} \circ \boldsymbol{A})\boldsymbol{R}_S(\boldsymbol{\alpha} \circ \boldsymbol{A})^H + \sigma^2\boldsymbol{I}, \qquad (30)$$

where σ^2 is the noise power at receiver sensors. Providing that the source signals are uncorrelated we have $\boldsymbol{R}_S = diag[P_1, \ldots, P_K]$ and the elements of $\boldsymbol{R}$ will be

$$r_{uv} = \sum_{k=1}^{K} \alpha_{uk}\alpha_{vk}^* a_{uk}a_{vk}^* P_k + \delta(u - v)\sigma^2, \qquad (31)$$

where $u, v = 1, \ldots, U$ and $k = 1, \ldots, K$. Considering (29), the statistical expectation of (31) with respect to α_{uk} will be

$$\mathbb{E}\{r_{uv}\} = \sum_{k=1}^{K} \mathbb{E}\{\alpha_{uk}\alpha_{vk}^*\}a_{uk}a_{vk}^* P_k + \delta(u - v)\sigma^2, \qquad (32)$$

where

$$\mathbb{E}\{\alpha_{uk}\alpha_{vk}^*\} = 1 + \delta(u - v)\sigma_f^2, \qquad (33)$$

with σ_f as fading depth, and therefore we have

$$\mathbb{E}\{r_{uv}\} = \sum_{k=1}^{K} a_{uk}a_{vk}^* P_k + \delta(u - v)\sigma^2$$

$$+ \delta(u - v)\sigma_f^2 \sum_{k=1}^{K} |a_{uk}|^2 P_k, \qquad (34)$$

in which the fading depth σ_f appears only on the last term. Therefore, we can rewrite (34) in a more compact form as

$$\mathbb{E}\{\boldsymbol{R}\} = \mathfrak{R} + \sigma_f^2\boldsymbol{P}, \qquad (35)$$

where $\mathfrak{R}$ is the fading-free covariance matrix we are looking for that equals the sum of first and second terms of (34), and $\boldsymbol{P} = diag([P_1, \ldots, P_U])$, where $P_u = \sum_{k=1}^{K} |a_{uk}|^2 P_k$ equals the fading-free total received power at u-th sensor. Assuming the same $P_u = P$ for all receiver sensors, we have $\boldsymbol{P} = P\boldsymbol{I}$. Approximating the expected covariance matrix $\mathbb{E}\{\boldsymbol{R}\}$ by averaging over $\boldsymbol{R}$ for N_e consecutive estimation intervals, during each of which the $\boldsymbol{\alpha}_n$ matrix can be assumed constant ($n = 1, \ldots, N_e$), we get

$$\bar{\boldsymbol{R}} \triangleq \frac{1}{N_e} \sum_{n=1}^{N_e} \boldsymbol{R}_n = \boldsymbol{R} + \sigma_f^2 P\boldsymbol{I}. \qquad (36)$$

We notify that the Eigen vectors of $\mathbb{E}\{\boldsymbol{R}\}$ are the same as those of $\mathfrak{R}$ but their Eigen values differ by $\sigma_f^2 P$, which means that fading acts the same as a noise with power $\sigma_f^2 P$. Moreover, notice that averaging over covariance matrix $\bar{\boldsymbol{R}}$ is the fastest solution to reduce the fading effect compared to the two aforementioned techniques, since it needs only one pass of the DPD algorithm after computing $\bar{\boldsymbol{R}}$.

VII. THE EFFECTS OF THE HUMAN BODY ON WAVE PROPAGATION

Radio wave propagation through the human body leads to the refraction and also attenuation that change both phase and amplitude of the received signal at receiver sensors. Here, we focus on the refraction phenomenon.

A. REFRACTION

According to the Snell's law, changing the propagation environment causes the a traveling wave to be refracted. More precisely, the Snell's Law states that

$$n_i \sin\theta_i = n_o \sin\theta_o, \qquad (37)$$

where n is the environment refraction index, θ indicates the incidence or refraction angle with respect to the normal vector
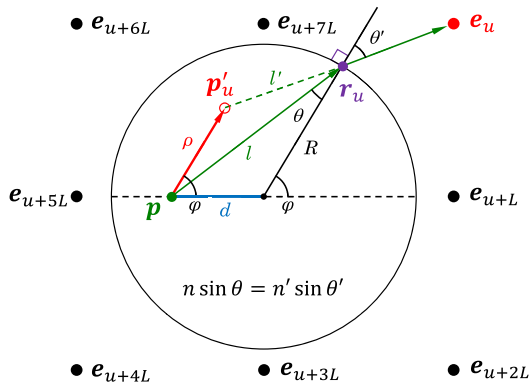
FIGURE 11. Basic parameters defined to determine the virtual displacement of point p to p'_u caused by refraction for element e_u; corresponding elements in surrounding column arrays are displayed.

of medias' boundary, and the subscripts i and o here denote *inside* and *outside* of the human body, respectively. For an electromagnetic wave, we have $n_o = 1.0$ and $n_i = 1.4$ [2]. In fact, the refraction phenomenon produces an *intrinsic bias* in a radio location problem, which means that if we don't regard the refraction in our localization algorithm, the signal source inside the human body *can never be seen on its true place*, even for a noise-free estimation.

FIGURE 11 depicts a 2D schema of the virtual emitter displacement from coordinates p to p'_u, seen by the u-th sensor element, due the refraction phenomenon. Considering our discussion on a cylindrical model in Appendix B, and assuming an isotropic environment for human body, the final location resulting from averaging over displacement vectors corresponding to all U sensors is

$$\bar{p} = \sum_{1}^{U} p'_u. \tag{38}$$

Therefore, the refraction leads to an overall intrinsic bias of

$$B_r(p) \triangleq \bar{p} - p. \tag{39}$$

Considering the array symmetry and a noise-free localization for a transmitter located at distance d from the cylinder axis, we have

$$B_r(p) = B_r(d) = \bar{d} - d, \tag{40}$$

where $\bar{d}$ is the noise-free estimate of location. The bias value is a function of d as explained in Appendix B.

B. METHOD1: REFRACTION PRE-CANCELLATION
Here, we present a perfect solution for DPD of WCE while taking into account the refraction phenomenon that virtually changes the path-lengths for traveling waves. This solution is based on the modification of pointing vector (a) in (23) to *compensate* the refraction effect.

FIGURE 12 depicts the wave refraction path using a cylindrical model for the human body. The signal is emitted from a
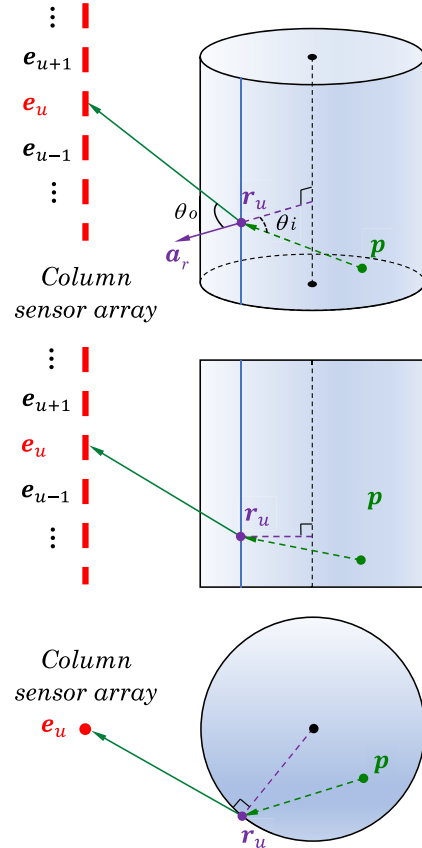

FIGURE 12. 3D and 2D refraction schema of wave emitted from WCE on p, refracted on r_u at cylinder surface, and reached the u-th sensor element on e_u.

hypothetical transmitter located at p, hits the cylinder surface at r_u on angle θ_i, leaves the surface on angle θ_i, and finally reaches the sensor element at e_u. The a_r is the outward-pointing, unit radial vector of cylinder at r_u. We indicate the plane containing $\{p, r_u, e_u\}$ as the refraction plane.

To analyze the effect of the human body on localization problem, we remember that refraction affects both phase and amplitude responses of the channel between the transmitter (WCE) and the receiver sensor. In other words, refraction changes the elements of the *pointing matrix A* in (5) that plays an essential role in the localization problem. Notice that the wave propagation speed depends reciprocally on the refraction index of the environment, despite of the carrier frequency which is constant. Thus, λ which has a key role in characterizing the channel phase response, depends on the refraction index. In fact, this is the basis of the Snell's Law is

$$\frac{v_o}{v_i} = \frac{\lambda_o}{\lambda_i} = \frac{n_i}{n_o} = n_i, \tag{41}$$

where v stands for the wave propagation speed, and the subscripts have the same definition as those in (37). It is worth mentioning that the refraction plane contains the cylinder radius on point r_u as a line segment. Considering the refraction path in FIGURE 12, we can determine the channel phase

response between WCE and u-th sensor element as

$$\check{\delta}_u = 2\pi \left(\frac{\|r_u - p\|}{\lambda_i} + \frac{\|e_u - r_u\|}{\lambda_o} \right),$$
$$= \frac{2\pi}{\lambda_o} (n_i\, d_{ui} + d_{uo}) = \frac{2\pi}{\lambda_o} \check{d}_u, \qquad (42)$$

where $d_{ui} = \|r_u - p\|$, $d_{uo} = \|e_u - r_u\|$, and $\check{d}_u$ is the virtual distance between signal emitter at p and receiver element at e_u. By comparing $\check{\delta}_u$ to the free space phase response, we have

$$\delta_u = \frac{2\pi}{\lambda_o} \|e_u - p\| = \frac{2\pi}{\lambda_o} d_u. \qquad (43)$$

To take the refraction effect into account, the elements of the pointing matrix A should be revised to $\check{A}$, by replacing δ_u with $\check{\delta}_u$ in (3). The coordinates of r_u are determined by minimizing the cost function

$$C(r_u) = \left| n_i \frac{\|(r_u - p) \times a_r\|}{\|r_u - p\|} - n_o \frac{\|(e_u - r_u) \times a_r\|}{\|e_u - r_u\|} \right|, \qquad (44)$$

obtained from (37) by scanning r_u on the cylinder surface. The cost function (44) is a more general form of the one presented in [2]. Unfortunately, there is no guaranty for the cost function (44) to have a valid minimum on the cylinder surface since the refraction prevents the emitted wave from any hypothetical point inside the cylinder to reach any arbitrary point outside. This means that some regions inside the cylinder are invisible to a sensor element. Fortunately, these regions have deterministic boundaries, which we investigate in Subsection VII-C.

C. HIDDEN AREAS: A CONSEQUENCE OF REFRACTION
Consider FIGURE 13, which shows a horizontal cut of the cylindrical model of human body. If a transmitter is located at the hashed regions, the sensor element at e_u receives no signals from that transmitter, since the most lateral beam that reaches e_u, is the one that hits the surface from the circle inside at *critical* angle ($\theta_i = \theta_{cr}$) and leaves that tangentially ($\theta_o = 90°$). By definition, we have $\theta_{cr} \triangleq \sin^{-1}(\frac{1}{n_i})$, which is about 46° for human body. In a more complex case, for a non-horizontal refraction plane with tilt angle η, we have

$$\tan \theta'_i = \cos \eta \, \tan \theta_i \qquad (45)$$

where θ'_i is the horizontal projection of θ_i. This means that other sensor elements in the same column as e_u will have hidden areas with larger horizontal projection segments than that depicted in FIGURE 13. Obviously, this leads to deterioration of WCE localization performance due to the wrong DOA data grabbed from blind sensors.

To have a successful localization, it is necessary to determine all the sensor elements that cannot see the search point p (for all GDPD, CDPD, and DOA-based techniques), and then ignore those blind sensors observations to remove the irrelative data throughout the algorithm. To do this, a prior knowledge about the position and orientation of patient's body is necessary, which is gradually achieved during iterations of the algorithm mentioned in FIGURE 3.
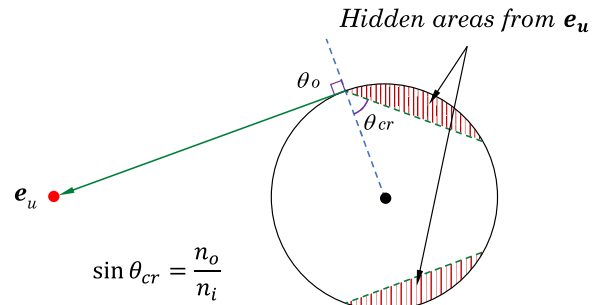

FIGURE 13. An instance of hidden areas due to refraction on critical angle θ_{cr} as an upper limit for inside incidence angle, which determines the hidden areas boundaries.
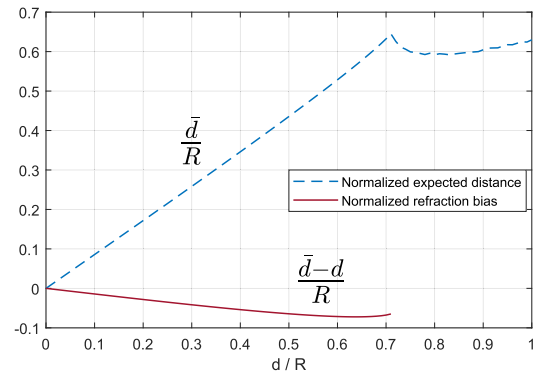

FIGURE 14. Normalized values of the estimated distance of the WCE from the body (cylinder with radius R) axis and its bias caused by the refraction phenomenon.

D. METHOD2: REFRACTION POST-CANCELLATION
In the tradeoff between the accuracy and simplicity, sometimes we prefer to have a lower computational load method even with lower performance. In fact, the pre-cancellation algorithm presented in Subsection VII-A consumes heavy computational resources. Therefore, we concentrate on the refraction post-cancellation idea, based on the removing of deterministic bias in (39). We analytically calculate the bias values with an acceptable resolution of d for only one time, and store them in a look-up-table (LUT). FIGURE 14 depicts the normalized value of the bias for an applicable range. Hence, to achieve a low computational load method, we localize the WCE ignoring the refraction effect, and then cancel the bias using the LUT. Notice that the bias LUT values are applicable as long as $\bar{d}$ is an invertible function of d. The aforementioned range $(0 \ldots 0.71R)$ seems realistic for the dimensions of intestine inside the body frame.

VIII. SIMULATIONS AND NUMERICAL RESULTS
Here, we investigate the improvement brought by using GDPD compared to CDPD and DOA-base localization techniques in a medical lab. The results of DOA-based methods can also be found in [1]–[3], [6]. We use the MUSIC beamformer for our simulations. The main parameter in our analysis is *3D location root-mean-square-error (RMSE)*
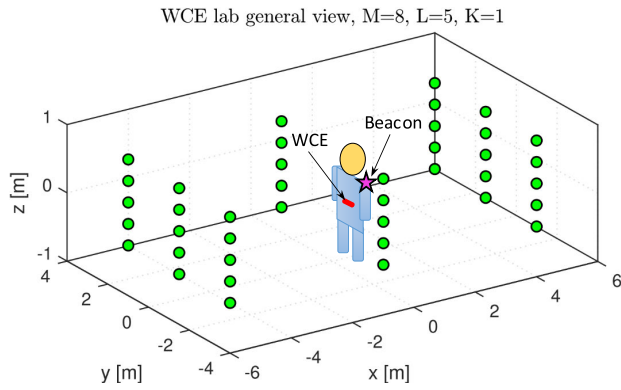
FIGURE 15. The plan of WCE lab for a 3D localization using C/GDPD for a single transmitter; the array dimensions are 5 m × 10 m × 2.5 m with the point (0, 0, 0) m at the array center. Elements vertical spacing is 3λ (BL = 3).

FIGURE 16. The superiority of GDPD over CDPD and DOA-based localization at the corner point (2, 0.4, 0) m of the patient walking area.

normalized to λ. Our results are averaged by using 100 Monte-Carlo experiments. There are 64 signal observations for each sensor element. The localization error is defined as the Euclidean distance between estimated location $\hat{p} = (\hat{x}, \hat{y}, \hat{z})$ and known positions of target at $p = (x, y, z)$ as

$$\epsilon \triangleq \|\hat{p} - p\|. \qquad (46)$$

We assume that the patient can walk through a determined area that guarantees the far-filed radiation conditions for both the WCE and beacons transmitting signals at carrier frequency 1430 MHz leading to wavelength as $\lambda \simeq 21$ cm. The standard frequency ranges 1395-1400 MHz or 1427-1432 MHz are approved by FCC Wireless Medical Telemetry Service (WMTS) [2], [28].

To show the vantage of exploiting our previously proposed DSAR technique [22], we consider both cases of having one and/or two transmitters ($K = 1, 2$). Notice that DPD methods are capable to locate co-channel signal sources. FIGURE 15 shows the map of the considered WCE lab with an 40-element SGA array ($M = 8, L = 5$) and vertical elements spacing BL = 3λ. We perform our numerical analysis for the point at coordinates (2,0.4,0)m on the *corner* of the patient walking area.

A. CASE OF ONE TRANSMITTER (K = 1)

FIGURE 16 depicts the performance of GDPD, CDPD, and DOA-based localization methods. It can be easily seen that GDPD outperforms CDPD and DOA-based method by about 12 dB and 15 dB, respectively. It is obvious that for SNR = 10dB as a practical condition, the normalized location RMSE is about −13 dB (1.05 cm) for CDPD, and about −25 dB (0.07 mm) for GDPD, which confirms the drastically higher performance brought by GDPD. It can be seen that when $K = 1$, there is no need to use DSAR since the results are enough close to their LBs.

B. CASE OF TWO TRANSMITTERS (K = 2)

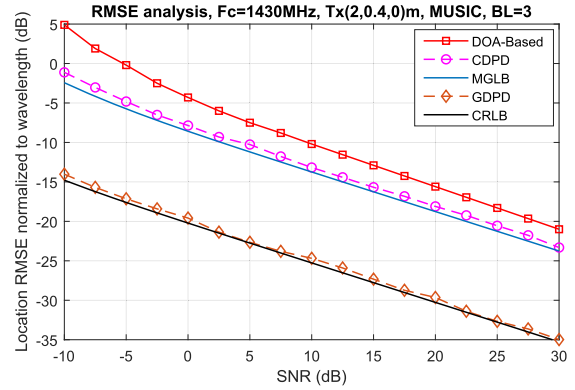In this case, we suppose two signal transmitters, namely a WCE inside the patient's intestinal path, and a beacon
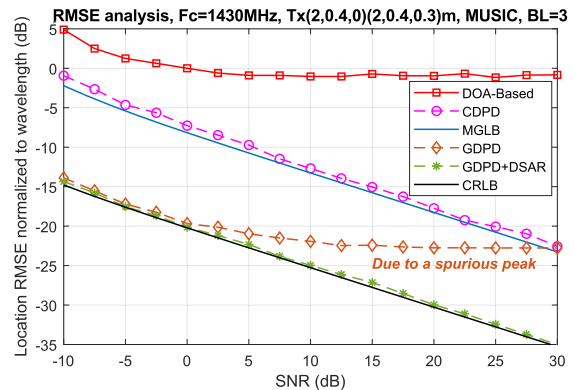

FIGURE 17. Failure of DOA-based localization, and the superiority of GDPD over CDPD for two transmitters (K = 2) at points (2, 0.4, 0) m and (2, 0.4, 0.3) m of monitoring area; DSAR brings a spur-free GDPD.

mounted on his shoulder, transmitting uncorrelated signals simultaneously. We assume about 30 cm ($\simeq 1.4\lambda$) of vertical distance between these two transmitters, which is a harsh condition for localization. The simulation results are provided in FIGURE 17 for a WCE located at (2,0.4,0)m and a beacon located at (2,0.4,0.3)m.

It can be seen that DOA-based localization method fails while facing with more than one signal emitter. For CDPD, there is no significant changes in the results comparing to the case of having only one signal emitter. Regarding GDPD, in contrast to the case of $K = 1$, we observe that without applying DSAR, the GDPD is trapped to a fixed normalized RMSE of about -23 dB. This phenomenon is related to spurious peaks generated in SPF which prevent the algorithm to find the true peak on the target position. Applying DSAR technique combats the undesirable spurious peaks around the target, and brings the RMSE to its predictable values.

C. ANALYZING THE FADING EFFECT

Here, we consider that the transmitter is located at point (2,0.4,0)m and our results are averaged over 100 realizations where $\sigma_f = 0.1$. FIGURE 18 shows the performance of our proposed averaging techniques to decrease the fading effect for DPD algorithm. It can be seen that
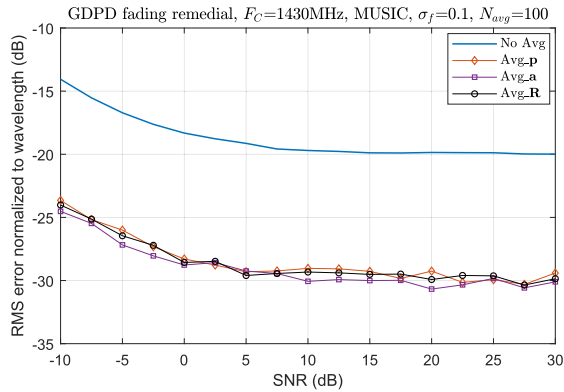
FIGURE 18. Decreasing the fading effect for MUSIC beamformer by averaging method over estimated position p, estimated pointing vector a, and covariance matrix R.

TABLE 1. Computations complexity for MUSIC algorithm's stages ($N_{it} = 100$ iterations, $N = 64$ samples, $U = 40$ sensors, $N_p = 15652$ monitoring points).

Item	Complexity Order
R	$O(N) \times O(U^2)$
EVD (Jacobi)	$N_{it} \times O(U^4)$
SPF	$N_p \times O(U^2)$

TABLE 2. Computational complexity of fading removal methods vs. MUSIC algorithm's stages ($N_{avg} = 100$).

Method	R	EVD	SPF
Avg_p	N_{avg}	N_{avg}	N_{avg}
Avg_a	N_{avg}	N_{avg}	N_{avg}
Avg_R	N_{avg}	1	1

the proposed averaging techniques reduce considerably the RMSE. Although the proposed methods perform almost similarly, it is worth mentioning that averaging over covariance matrix R has the lowest computational burden. Tables 1 and 2 show the complexity of operations for fading removal methods.

D. ANALYZING THE REFRACTION EFFECT

In this part, we numerically investigate the effect of refraction phenomenon on the performance of CDPD for three cases: without cancellation, pre-cancellation, and post-cancellation of refraction. FIGURE 19 depicts the value of localization RMSE normalized to wavelength ($\lambda \simeq 21$ cm), for the simulation of mentioned scenario. It can be seen that the refraction pre-cancellation method proposed in VII-B, performs such as the CDPD when there is no refraction effect. Furthermore, the refraction post-cancellation (low computational load) method proposed in VII-D, underperforms the previous technique for about 3 dB for SNR < 15 dB. For SNR $\geq$ 15 dB, this method cannot provide more accuracy because of the approximation error of bias cancellation. Of course, the value of -14 dB for normalized RMSE (about 1cm) is an acceptable accuracy
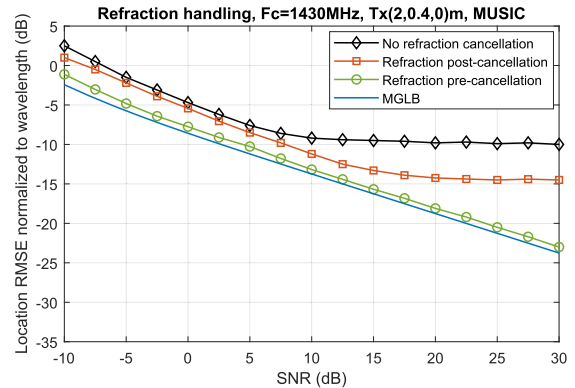

FIGURE 19. Comparing the refraction canceling techniques for a cylindrical model: no cancellation, post-cancellation, and pre-cancellation of refraction, MGLB.

to localize WCE for many cases. Finally, the localization method without refraction canceling is presented, whose performance is lower than two other methods as expected, where the normalized RMSE reaches -10 dB (about 2.1 cm) for SNR > 10 dB.

IX. CONCLUSION

The problem of WCE localization in WMTS labs using the combination of CDPD as a coarse (medium resolution) and GDPD as a fine (high resolution) position estimator was addressed. We showed that GDPD outperforms classical WCE localization methods in terms of accuracy (about 15dB) and capability to resolve more than one signal sources at the same time. We showed that our previously introduced technique DSAR [22] can significantly increase the robustness of GPDP while localizing several signal emitters (theoretically up to one less than the number of sensor elements in a group [13]).

We derived the CRLB formulation for SGA, and also introduced the MGLB for MGA structures, and showed that GDPD outperforms the CDPD for about 10-15 dB, depending on the location of WCE through the WMTS ward. In addition, we introduced two visual tools based on the CRLB value and also the mutual error distributions to achieve a proper geometry and elements arrangement for any arbitrary array.

Moreover, we provided a comprehensive analysis on wave refraction phenomenon in a WMTS lab due to tissue of human body, and pointed out the superiority of DPD over DOA-based localization methods in this sense by using the refraction pre-cancellation technique. We also proposed the refraction post-cancellation as a low computational load method, which of course has a lower accuracy than the former technique.

Finally, we proposed three techniques for different stages of DPD algorithm in order to combat the effect of channel fading. We particularly showed that averaging over the covariance matrix of array observations is the fastest and most effective way to reduce the destructive effects of the channel fading.

APPENDIX A
THEORETICAL RMSE LOWER BOUNDS CORRESPONDED TO SGA AND MGA STRUCTURES

We derive the CRLB for DPD problem considering an arbitrary point p in a 3D monitoring area, knowing the geometry of the receiving array and the location and signal power of some determined transmitters. To derive the CRLB expression, we consider the NB matrix form of SGA structure (GDPD) in (8) which leads to the covariance matrix $\boldsymbol{R}$ in (17). Then to obtain the MGLB for MGA structure (CDPD), we replace the $\boldsymbol{R}$ with its sparse version in (19) throughout the following relations. We assume a zero mean complex Gaussian distribution for each signal snapshot, conditioned to a known parameter vector ψ. The elements of the Fisher information matrix (FIM) are given by [13]

$$\boldsymbol{F}_{ij} = N \, tr \left(\boldsymbol{R}^{-1} \frac{\partial \boldsymbol{R}}{\partial \psi_i} \boldsymbol{R}^{-1} \frac{\partial \boldsymbol{R}}{\partial \psi_j} \right), \qquad (47)$$

$$= -N \, tr \left(\frac{\partial \boldsymbol{R}^{-1}}{\partial \psi_i} \frac{\partial \boldsymbol{R}}{\partial \psi_j} \right), \qquad (48)$$

where N is the number of observations of array signals, and ψ_i and ψ_j are the i-th and j-th elements of parameter vector ψ, respectively. To comply with 3D applications like WMTS and by assuming that fading coefficients are constant during one observation interval, we consider the unknown parameter $\psi = p = [x, y, z]^T$. Assuming that noises at receiver elements are uncorrelated and have the same power σ^2, we can rewrite (17) as

$$\boldsymbol{R} = \widetilde{\boldsymbol{A}} \boldsymbol{R}_S \widetilde{\boldsymbol{A}}^H + \sigma^2 \boldsymbol{I}_U = \boldsymbol{R}_A + \sigma^2 \boldsymbol{I}_U, \qquad (49)$$

from which the elements of $\boldsymbol{F}$ can be determined. To calculate $\boldsymbol{R}^{-1}$, according to the matrix inversion lemma we have

$$\boldsymbol{R}^{-1} = \sigma^{-2} \left(\boldsymbol{I}_U - \widetilde{\boldsymbol{A}} (\widetilde{\boldsymbol{A}}^H \widetilde{\boldsymbol{A}} + \sigma^2 \boldsymbol{R}_S^{-1})^{-1} \widetilde{\boldsymbol{A}}^H \right). \qquad (50)$$

For a single transmitter ($K = 1$) with power P, from (50) we get

$$\boldsymbol{R}^{-1} = \sigma^{-2} \boldsymbol{I}_U - \frac{\sigma^{-2} \tilde{a} \tilde{a}^H}{\|\tilde{a}\|^2 + \dfrac{\sigma^2}{P}}. \qquad (51)$$

On the other hand, derivation of (49) with respect to $\psi \in \{x, y, z\}$ leads to

$$\frac{\partial \boldsymbol{R}}{\partial \psi} = \frac{\partial \widetilde{\boldsymbol{A}}}{\partial \psi} \boldsymbol{R}_S \widetilde{\boldsymbol{A}}^H + \widetilde{\boldsymbol{A}} \boldsymbol{R}_S \frac{\partial \widetilde{\boldsymbol{A}}^H}{\partial \psi}. \qquad (52)$$

To compute the CRLB for localization of the k-th transmitter among K ones, i.e., $p = p_k$, we notice that all transmitters except the one at point p_k are considered to have stationary locations and so, we can ignore them during the derivation procedure. Then we have

$$\frac{\partial \widetilde{\boldsymbol{A}}}{\partial \psi} = \frac{\partial}{\partial \psi} [\tilde{a}_1, \dots, \tilde{a}_K] = \left[\boldsymbol{0}, \dots, \frac{\partial \tilde{a}_k}{\partial \psi}, \dots, \boldsymbol{0} \right]. \qquad (53)$$

For notation simplicity, we remove the subscript k to have $\tilde{a} = \tilde{a}_k$. Assuming that the emitted signal from p is uncorrelated to other emitter signals, we have

$$\frac{\partial \boldsymbol{R}}{\partial \psi} = \frac{\partial \tilde{a}}{\partial \psi} P \tilde{a}^H + \tilde{a} P \frac{\partial \tilde{a}^H}{\partial \psi} = P \frac{\partial}{\partial \psi} (\tilde{a} \tilde{a}^H), \qquad (54)$$

where P is the k-th diagonal element of $\boldsymbol{R}_S$ representing the transmitted power from point p that we assume it is normalized to one.

Considering (3), for the u-th element of $\tilde{a}$ we have

$$\tilde{a}_u = \alpha_u \, g_u \frac{d_0}{d_u} \, e^{-j \frac{2\pi}{\lambda} d_m}, \qquad (55)$$

$$\frac{\partial \tilde{a}_u}{\partial \psi} = -\left(\frac{1}{d_u} + j \frac{2\pi}{\lambda} \right) \tilde{a}_u \frac{\partial d_u}{\partial \psi}, \qquad (56)$$

where d_u is the distance between p and the u-th receiver element with

$$d_u^2 = (x - x_u)^2 + (y - y_u)^2 + (z - z_u)^2,$$
$$\frac{\partial d_u}{\partial \psi} = \frac{\psi - \psi_u}{d_u} = \cos \phi_{\psi u}, \qquad (57)$$

where $\phi_{\psi u}$ is the angle between ψ-axis and the line pointing p from the u-th element. We have

$$\frac{\partial \tilde{a}}{\partial \psi} = - \, diag(\boldsymbol{\zeta} \circ \cos \boldsymbol{\phi}_\psi) \tilde{a},$$
$$\frac{\partial \tilde{a}^H}{\partial \psi} = - \, \tilde{a}^H diag(\boldsymbol{\zeta}^* \circ \cos \boldsymbol{\phi}_\psi), \qquad (58)$$

where $\boldsymbol{\zeta} = [\zeta_1, \dots, \zeta_U]^T$, $\zeta_u = -(1/d_u + j2\pi/\lambda)$, $\boldsymbol{\phi}_\psi = [\phi_{\psi 1} \dots, \phi_{\psi U}]^T$. Using (54) and by analogy, we get

$$\frac{\partial \boldsymbol{R}}{\partial \psi} = P \, \boldsymbol{C}_\psi \circ (\tilde{a} \tilde{a}^H), \qquad (59)$$

where

$$\boldsymbol{C}_\psi \triangleq diag(\boldsymbol{\zeta} \circ \cos \boldsymbol{\phi}_\psi) \, \boldsymbol{1}_U + \boldsymbol{1}_U \, diag(\boldsymbol{\zeta}^* \circ \cos \boldsymbol{\phi}_\psi). \quad (60)$$

For a CDPD problem with M number of L-element independent arrays, we have

$$\boldsymbol{C}_\psi \triangleq diag(\boldsymbol{\zeta} \circ \cos \boldsymbol{\phi}_\psi) \, \boldsymbol{W} + \boldsymbol{W} \, diag(\boldsymbol{\zeta}^* \circ \cos \boldsymbol{\phi}_\psi), \quad (61)$$

where $\boldsymbol{W} = \boldsymbol{I}_M \otimes \boldsymbol{1}_L$. In fact, $\boldsymbol{W}$ *masks* any statistical dependency between observations at different arrays, which leads to a tighter LB due to the lack of mutual information between different arrays. Finally, we can compute the elements of $\boldsymbol{F}$ and consequently derive the CRLB or MGLB as $tr(\boldsymbol{F}^{-1})$. In this regard, we notify some important points, as follows.

- For an unbiased position estimate $\hat{p}$, we have

$$\epsilon_{rms}^2 = var(\hat{p}) \geq tr \left(\boldsymbol{F}^{-1} \right), \qquad (62)$$

  where ϵ_{rms} is the RMS of localization error.
- Due to the fading coefficients included in $\tilde{a}$, which are considered constant during one DPD estimation interval, we can average the LBs resulted from several random sets of fading coefficients to achieve a more reliable LB [29].

- The *total* SNR in (49) is calculated as

$$\text{SNR} = \frac{tr\,(\boldsymbol{R}_A)}{U\,\sigma^2}. \tag{63}$$

Moreover, the specific SNR related to the k-th transmitter, i.e., SNR_k, by using the properties of $tr()$ operator, as is given

$$\text{SNR}_k = \frac{tr\,\left(\boldsymbol{a}_k P_k \boldsymbol{a}_k^T\right)}{\sigma^2} = \frac{\boldsymbol{a}_k^T \boldsymbol{a}_k P_k}{\sigma^2}, \tag{64}$$

where P_k is the power of the k-th signal transmitter.

APPENDIX B
LOCALIZATION BIAS DUE TO REFRACTION

Considering the scenario depicted in FIGURE 11, we investigate the virtual displacement of the arbitrary point $\boldsymbol{p} = \boldsymbol{p}_u$ inside a circle with radius R due to the refraction phenomenon.

The wave radiated from $\boldsymbol{p}$ hits the perimeter of the circle at point $\boldsymbol{r}$ with angle θ and leaves $\boldsymbol{r}$ with refracted angle θ' according to the Snell's law, with refraction indices are $n > 1$ inside, and $n' = 1$ outside the circle, respectively. Therefore the point $\boldsymbol{p}$ with distance l from the refraction point $\boldsymbol{r}$ will be seen at the point $\boldsymbol{p}'$ with distance l' from $\boldsymbol{r}$. Now we find the displacement value ρ as a function of φ which is the central angle of refraction point $\boldsymbol{r}$. We have

$$l^2 = R^2 + d^2 + 2Rd\cos\varphi, \tag{65}$$

$$\cos\theta = \frac{R + d\cos\varphi}{l} \triangleq \frac{C_\varphi}{l},$$

$$\sin\theta = \frac{d\sin\varphi}{l} \triangleq \frac{S_\varphi}{l}. \tag{66}$$

Using some geometric rules, it can be easily shown that

$$\rho(\varphi) = R\left(1 - \frac{\sin(\varphi - \theta)}{n\sin(\varphi - \theta')}\right). \tag{67}$$

Considering (65) and specially the definitions in (66), and using some trigonometrical manipulations, (67) can be written as

$$\rho(\varphi) = C_\varphi - \frac{1}{n}\sqrt{C_\varphi^2 - (n^2 - 1)S_\varphi^2}. \tag{68}$$

FIGURE 20 depicts $\rho(\varphi)$ for three different values of d, which is the distance between $\boldsymbol{p}$ and the center of circle. In the first case (rightmost) where $d = 0$, we get a circle that is concentric with body circle, which makes no localization bias. In the second case, where $d = 0.3R$, we get a convex connected shape with a little bias or distance between real location and estimated one as shape's centroid. The third case, where $d = 0.5R$, generates a concave closed shape with larger bias compared to the first one. Finally, the last case with $d = 0.8R$ produces a concave open curve with a very larger bias than the two former cases. The open parts of curve are related to the situations where the emitter is located at hidden areas as described in Section VII-C and depicted in FIGURE 13.

Finally, assuming the array symmetry such as in FIGURE 11, the refraction intrinsic bias in (39) equals $\bar{d} - d$,
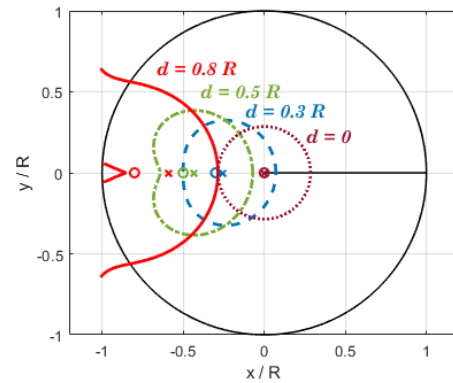

FIGURE 20. Loci of p' due to the refraction, for four arbitrary values of *d* and $0 \le \varphi < 2\pi$ and; the little colorful circles show the given *p* locations, and little crosses with proportional colors show the $\bar{p}$ positions (centroids of p' loci) as the biased emitter locations.

where $\bar{d}$ is the distance of the centroid of $\boldsymbol{p}'$ locus, from the cylinder axis. Unfortunately the integral of the function in (68) cannot be derived analytically with respect to φ, so we should use the numerical averaging to calculate the estimation bias.

REFERENCES

[1] Y. Ye, U. Khan, N. Alsindi, R. Fu, and K. Pahlavan, "On the accuracy of RF positioning in multi-capsule endoscopy," in *Proc. IEEE 22nd Int. Symp. Pers., Indoor Mobile Radio Commun.*, Sep. 2011, pp. 2173–2177.
[2] S. T. Goh, S. R. Zekavat, and K. Pahlavan, "DOA-based endoscopy capsule localization and orientation estimation via unscented Kalman filter," *IEEE Sensors J.*, vol. 14, no. 11, pp. 3819–3829, Nov. 2014.
[3] A. Nafchi, S. T. Goh, and S. R. Zekavat, "Circular arrays and inertial measurement unit for DOA/TOA/TDOA-based endoscopy capsule localization: Performance and complexity investigation," *IEEE Sensors J.*, vol. 14, no. 11, pp. 3791–3799, Nov. 2014.
[4] H. Wang, Y. Zhang, X. Yu, and G. Wang, "Positioning algorithm for wireless capsule endoscopy based on RSS," in *Proc. IEEE Int. Conf. Ubiquitous Wireless Broadband (ICUWB)*, Nanjing, China, Oct. 2016, pp. 1–3.
[5] Y. Xu and M. Q.-H. Meng, "Free sensor array based relative localization system for wireless capsule endoscopy," in *Proc. IEEE Int. Conf. Robot. Biomimetics (ROBIO)*, Dec. 2018, pp. 550–555.
[6] U. Khan, Y. Ye, A.-U. Aisha, P. Swar, and K. Pahlavan, "Precision of EM simulation based wireless location estimation in multi-sensor capsule endoscopy," *IEEE J. Transl. Eng. Health Med.*, vol. 6, pp. 1–11, 2018.
[7] A. J. Weiss, "Direct position determination of narrowband radio frequency transmitters," *IEEE Signal Process. Lett.*, vol. 11, no. 5, pp. 513–516, May 2004.
[8] A. J. Weiss and A. Amar, "Direct position determination of multiple radio signals," *EURASIP J. Adv. Signal Process.*, vol. 2005, no. 1, pp. 37–49, Dec. 2005.
[9] T. Tirer and A. J. Weiss, "High resolution direct position determination of radio frequency sources," *IEEE Signal Process. Lett.*, vol. 23, no. 2, pp. 192–196, Feb. 2015.
[10] L. Tzafri and A. J. Weiss, "High-resolution direct position determination using MVDR," *IEEE Trans. Wireless Commun.*, vol. 15, no. 9, pp. 6449–6461, Sep. 2016.
[11] T. Tirer and A. J. Weiss, "Performance analysis of a high-resolution direct position determination method," *IEEE Trans. Signal Process.*, vol. 65, no. 3, pp. 544–554, Feb. 2017.
[12] C. Qian, L. Huang, Y. Xiao, and H. C. So, "Localization of coherent signals without source number knowledge in unknown spatially correlated Gaussian noise," *Signal Process.*, vol. 111, no. 2, pp. 170–178, Jun. 2015.
[13] H. L. V. Trees, *Optimum Array Processing*. New York, NY, USA: Wiley, 2002, ch. 8.

[14] C. M. N. Brigante, N. Abbate, A. Basile, A. C. Faulisi, and S. Sessa, "Towards miniaturization of a MEMS-based wearable motion capture system," *IEEE Trans. Ind. Electron.*, vol. 58, no. 8, pp. 3234–3241, Aug. 2011.

[15] T. Iida, D. Anzai, and J. Wang, "Performance evaluation on WCE localization using GA-based three-dimensional electromagnetic imaging," in *Proc. 10th Int. Symp. Med. Inf. Commun. Technol. (ISMICT)*, Mar. 2016, pp. 1–5.

[16] H. Mateen, R. Basar, A. U. Ahmed, and M. Y. Ahmad, "Localization of wireless capsule endoscope: A systematic review," *IEEE Sensors J.*, vol. 17, no. 5, pp. 1197–1206, Mar. 2017.

[17] I. Umay, B. Fidan, and B. Barshan, "Localization and tracking of implantable biomedical sensors," *Sensors*, vol. 17, no. 3, pp. 583–602, 2017.

[18] F. Bianchi, A. Masaracchia, E. Shojaei Barjuei, A. Menciassi, A. Arezzo, A. Koulaouzidis, D. Stoyanov, P. Dario, and G. Ciuti, "Localization strategies for robotic endoscopic capsules: A review," *Expert Rev. Med. Devices*, vol. 16, no. 5, pp. 381–403, May 2019.

[19] A. Weiss, "Direct geolocation of wideband emitters based on delay and Doppler," *IEEE Trans. Signal Process.*, vol. 59, no. 6, pp. 2513–2521, Jun. 2011.

[20] O. Bar-Shalom and A. J. Weiss, "Efficient direct position determination of orthogonal frequency division multiplexing signals," *IET Radar, Sonar Navigat.*, vol. 3, no. 2, pp. 101–111, Apr. 2009.

[21] L. Huang and Y. Lu, "Performance analysis of direct position determination for emitter source positioning," *Amer. J. Signal Process.*, vol. 2, no. 3, pp. 41–45, Aug. 2012.

[22] A. Eshkevari and S. M. S. Sadough, "Enhanced direct position determination using dynamic sensor array response," *Electron. Lett.*, vol. 56, no. 7, pp. 354–357, Mar. 2020.

[23] J. Capon, "High-resolution frequency-wavenumber spectrum analysis," *Proc. IEEE*, vol. 57, no. 8, pp. 1408–1418, Aug. 1969.

[24] D. H. Brandwood, "A complex gradient operator and its application in adaptive array theory," *IEE Proc. H-Microw., Opt. Antennas*, vol. 130, no. 1, pp. 11–16, 1983.

[25] G. V. Borgiotti and L. Kaplan, "Superresolution of uncorrelated interference sources by using adaptive array techniques," *IEEE Trans. Antennas Propag.*, vol. 27, no. 6, pp. 842–845, Nov. 1979.

[26] W. F. Gabriel, "Spectral analysis and adaptive array superresolution techniques," *Proc. IEEE*, vol. 68, no. 6, pp. 654–666, Jun. 1980.

[27] R. O. Schmidt, "Multiple emitter location and signal parameter estimation," *IEEE Trans. Antennas Propag.*, vol. I-34, no. 3, pp. 276–280, Mar. 1986.

[28] F.C.C., *Regulations for Title 47 C.F.R*, FCC Rules, document 95, 2019.

[29] O. Bar-Shalom and A. J. Weiss, "Direct positioning of stationary targets using MIMO radar," *Signal Process.*, vol. 91, no. 10, pp. 2345–2358, 2011.

ALI ESHKEVARI was born in Tehran, Iran, in 1968. He received the B.Sc. degree in electrical engineering (electronics) from the Khajeh Nasir Toosi University of Technology, Tehran, in 1991, and the M.Sc. degree in electrical engineering (telecommunication systems) from the Amirkabir University of Technology, Tehran, in 1997. He is currently pursuing the Ph.D. degree with the Electrical Engineering Department, Shahid Beheshti University, Tehran. His Ph.D. thesis is on direct position determination of radio signals.

SEYED MOHAMMAD SAJAD SADOUGH was born in 1979. He received the B.Sc. degree in electrical engineering (electronic) from Shahid Beheshti University, Tehran, Iran, in 2002, and the M.Sc. and Ph.D. degrees in electrical engineering (telecommunication) from Paris-Saclay University, Orsay, France, in 2004 and 2008, respectively.

During his Ph.D. (2004–2007), he was with the Institut Polytechnique de Paris (ENSTA), Paris, France, and CentraleSupélec—CNRS/Laboratory of Signals and Systems (LSS), Gif-sur-Yvette, France. He has been a Lecturer with the Electronics and Computer Engineering Department, ENSTA, where his research activities were focused on improved reception schemes for ultra wideband communication systems. From December 2007 to September 2008, he was a Postdoctoral Researcher at CentraleSupélec—CNRS/LSS, where he was involved in research projects with Alcatel-Lucent on satellite mobile communication systems. In October 2008, he joined the Faculty of Electrical Engineering, Shahid Beheshti University, where he is currently an Associate Professor with the Telecommunication Department. His current research interests include optical wireless communications, signal processing for wireless communications, with particular emphasis on multicarrier and MIMO systems, joint channel estimation and decoding, iterative reception schemes, and receiver design under partial channel state information.

• • •